

Effect of fibers and boron carbide on the radiation shielding properties of limestone and magnetite aggregate concrete

S. Pérez^a, P. Tamayo^{b,*}, J. Rico^a, J. Alonso^a, C. Thomas^b

^a Construction Engineering, Research and Project Development (INGECID S.L.), University of Cantabria. E.T.S. de Ingenieros de Caminos, Canales y Puertos, Av./Los Castros 44, 39005, Santander, Spain

^b LADICIM (Laboratory of Materials Science and Engineering), University of Cantabria. E.T.S. de Ingenieros de Caminos, Canales y Puertos, Av./Los Castros 44, 39005, Santander, Spain

ARTICLE INFO

Keywords:

Radiation shielding concrete
PVA fibers
Steel fibers
Boron carbide
Magnetite
Simulations
Neutron
Gamma

ABSTRACT

Research on new composite materials in the field of radiation shielding materials requires adequate means and meticulousness in their manufacture and characterization. In this study, concretes that use elements that theoretically improve their shielding properties are developed, such as fibers and boron-rich additions. Both magnetite and limestone concrete have been manufactured, incorporating steel fibers to improve the linear attenuation coefficient and polyvinyl alcohol to increase neutron scattering cross section. The incorporation of boron carbide is intended to increase the neutron absorption cross section. 5 mixes have been manufactured that have been tested with several gamma radiation sources (570–1280 keV) and with an Am–Be neutron source (111 GBq). The experimental results have been used to validate simulations carried out with MAVRIC® and have led to the modelling of a simplified spent nuclear fuel cask. Boron carbide produces a decrease of more than 50% on the neutron dose rate in contact with the cask. Incorporating PVA fibers supposes gain in neutron attenuation capacity of up to 13%, while fibers have a negligible effect on the photon dose rate.

1. Introduction

Concrete is the most widely used radiation shielding material (Singh et al., 2015), it does not suffer from corrosion, it is versatile, available anywhere (Tyagi et al., 2020), it requires little maintenance (Mehta and Monteiro, 2006), it is effective at attenuating both gamma and neutron radiation (El-Sayed Abdo, 2002) and has the advantage with respect to lead that it is non-toxic, it is cheap and easy to use (Kaplan, 1989).

Gamma radiation and neutron radiation are the two primary forms of ionizing radiation. Gamma ray attenuation (photon attenuation) through a material occurs exponentially with absorber thickness and it is governed by Lambert's Law (Kazjonovs et al., 2010). The most effective materials in photon attenuation are high-density materials, as they have a high linear attenuation coefficient (μ). In the case of concrete, it is possible to increase the density using ferrous aggregates such as magnetite, goethite (Thomas et al., 2019a, 2021) or even siderurgical aggregates (Tamayo et al., 2022) and barite (Al-Ghamdi et al., 2022), allowing the density of the concrete to be increased between 3 and 4 g/cm³. Recent investigations have demonstrated the feasibility of copper slags (Ameri et al., 2020), increasing μ by 42% for a 60% substitution

of the aggregate, and the efficacy of using ferrophosphorus aggregates and metal dust waste, materials that reach a density of ~ 5.5 g/cm³ (Suwanmaneechot et al., 2021), have also been validated. Some other ferrous bodies such as iron punchings and balls have also been encapsulated in the cement matrix to increase the density of the mix (Kazjonovs et al., 2010; Peng and Hwang, 2011), although the ideal would be to incorporate a material that, in addition to providing density, would contribute to the mechanical performance of the concrete. Here the metallic fibers appear, which in addition to providing density prevent brittle failure and improve the splitting tensile and flexural strength of concrete (Khaloo et al., 2014).

On the other hand, the neutron attenuation is not purely exponential with absorber thickness due to the influence of neutrons scattered in the shielding and, to a lesser extent, in the air. The most effective materials in neutron attenuation are light nuclei materials, as they have a high neutron scattering cross sections (Σ) (Kaplan, 1989). Thus, materials with a high H content are the most effective at attenuating fast neutrons. In the case of concrete, the main H supplier is the hydrated cement (Tamayo et al., 2022), although polymeric materials such as polypropylene (PP) (Çakırouglu, 2016) or polyvinyl alcohol (PVA) (Thomas

* Corresponding author.

E-mail address: tamayop@unican.es (P. Tamayo).

et al., 2019b) fibers, which are $-CH-$ chains. Once attenuated or thermalized, neutrons are captured by materials with large absorption cross section by radiative capture. The most effective common materials absorbing thermalized neutrons are boron and cadmium (Tamayo et al., 2020) and in concrete, aggregates that naturally incorporate boron such as colemanite (Yarar and Bayülken, 1994) or ferroboration (Roslan et al., 2019; Sarkawi et al., 2018). However, an interesting option would be to incorporate into the concrete additions that have proven to be highly effective in other composites, such as boron carbide (B_4C). On the other hand, it can be reasoned that elements that improve both the thermalization of neutrons and the capture of thermalized neutrons are light elements, whose use entails the reduction of the gamma radiation shielding capacity.

In this research it is intended to quantify, in terms of radiological shielding capacity, the effect of incorporating fibers, both polymeric and metallic, in concrete (limestone and magnetite aggregates concrete). In addition, the effect of simultaneously incorporating B_4C filler, a novel addition already used in steels and polymeric compounds, will be evaluated. For this, an ambitious methodological program has been proposed consisting of the characterization of 5 different concrete mixes in an experimental set-up for gamma and for neutron radiation shielding tests. These tests make it possible to compare the different materials and to validate the simulations performed using MAVRIC® models of the experimental devices. With the validated simulations, a simplified model of a spent nuclear fuel cask will be created, which will allow to compare dose rates obtained with the different mixes as a cask shielding.

2. Methodology

2.1. Materials and mix proportions

For the manufacture of the 5 concrete mixes, both natural limestone aggregates (NA) and magnetite aggregates (MA) have been used. Additions used include limestone filler (LF) and boron carbide filler (BF). The purity of BF is close to 99% and the shape of the particles is angular cubic. Table 1 shows the physical properties of these materials, including the bulk, apparent and saturated surface dry (SSD) densities (EN 1097-3 (British Standards Institution, 1998)), as well as the porosity and water absorption (EN 1097-6 (E.N. 1097-6:2014, 2014)). It is worth noting the difference in terms of density between the two types of aggregates, being 45% higher in the case of MA.

Two types of fibers have been used: polyvinyl alcohol (PVA) fibers and steel fibers (SF). The steel fibers meet the requirements established in EN 14889-1 (AENOR, 2008a), they are straight, the tensile strength is 2850 MPa and they have a copper-zinc coating (brass) in the proportions 70-30% respectively. PVA fibers meet the requirements established in EN 14889-2 (AENOR, 2008b), they are straight, their composition (C_2H_4O) should favor the attenuation of fast neutrons and the tensile strength is 750 MPa. Fig. 1 shows some of the main fiber characteristics, including density (d), average diameter (D_m), and average length (L_m).

The concrete was manufactured in a planetary mixer with a vertical axis, with a capacity of 150 l, pouring the aggregates from largest to

Table 1
Physical properties of the aggregates used.

Component (mm/mm)	Bulk density [g/cm ³]	Apparent density [g/cm ³]	SSD density [g/cm ³]	Water absorption [% wt.]	Porosity [% vol.]
NA 12/20	2.65	2.76	2.69	1.6	4.2
NA 6/12	2.67	2.78	2.71	1.4	3.7
NA 0/6	2.67	–	–	–	–
MA 0/20	4.76	5.05	4.82	1.2	5.7
MA 0/8	4.76	5.00	4.83	1.0	4.8
LF	2.70 ^a	–	–	–	–
BF	2.57 ^a	–	–	–	–

^a Bulk density is the actual density for filler particles.

smallest size and finally the cement and additions. The batches were 100 l, carried out in three phases: 3 min of kneading, 3 min of rest and 2 min of kneading incorporating the superplasticizer additive (SP). Factors related to environmental conditions are those related to the laboratory, whose ambient temperature ranges from 18 to 22 °C and humidity is in the range of 60–70%.

5 concrete mixes have been designed to establish the effect of aggregates, fibers, fiber types and boron carbide on the radiation shielding properties of concrete. The five mixes (Table 2) have been designed by the Fuller method using the similar amounts of water, cement (CEM I 52.5 R (E.N. 197-1:2011, 2011)), superplasticizer additive (SP) and volume of aggregates, to facilitate their comparison.

- L-LF-0: A reference limestone concrete mix with limestone filler and no fibers.
- L-LF-7P: A limestone concrete mix with limestone filler and 7 kg/m³ of PVA fibers.
- L-BF-7P: A limestone concrete mix with boron carbide filler and 7 kg/m³ of PVA fibers.
- M-0-7P: A magnetite concrete mix with 7 kg/m³ of PVA fibers.
- M-0-40S: A magnetite concrete mix with 40 kg/m³ of steel fibers (same volume as 7 kg/m³ of PVA fibers).

Table 2 shows the mix proportions of the mixes produced. In the coding, the type of aggregate is shown first (L: Limestone, M: magnetite), followed by the type of filler used (LF: Limestone, BF: boron carbide, 0: none) and finally the % wt. of fibers with the material of these (P: plastic, S: steel). The slump according to EN 12350-2 (E.N. 12350-2:2009, 2009) and the hardened density of concrete according to EN 12390-7 (E.N. 12390-7:2009, 2009) are also shown. The first is a fundamental parameter in terms of workability and placement of the concrete, while the second is essential to be able to carry out the theoretical simulations.

Fig. 2 shows the appearance of each mix in 100 × 100 mm plates. Visually, differences between the two types of aggregate used can be seen, but the fibers cannot be seen. On the other hand, among the concrete mixes that use limestone, the mix that incorporates BF shows a darker paste, due to the black color of the boron carbide powder. The other two mixes (M-0-7P and M-0-40S) also show a dark color, due to the ferrous nature of the magnetite. When cutting the plates, the resistance shown by this mix to cutting is striking, because boron carbide is the second hardest material after diamond.

The chemical composition of the concretes has been determined using the methodology recently developed by the authors in a previous study (Tamayo et al., 2022). The composition of the CEM has been determined from the hydration products, while that of the aggregates has been determined from X-Ray Fluorescence (XRF) using a Thermo model ARL-ADVANT-XP spectrometer. Table 3 shows the chemical composition of the 5 mixes developed. The composition of each mix is a fundamental input to perform Monte Carlo calculations.

2.2. Experimental set-ups

The experimental tests allow to establish the goodness of the simulations, taking direct measurements of the amount of particles that reach the detector when inserting a concrete shield. The objective of this experimentation is to validate the simulations, facing the results obtained by both ways. Having very similar results in both ways (experimental and simulations) will allow demonstrating the seriousness of the results obtained in this study and will open the door to the design of more complex geometries, such as spent nuclear fuel casks.

The experimental set-ups used are located in the Department of Modern Physics of the University of Cantabria. In the case of photon shielding evaluation (Fig. 3 left), the study of attenuation has been carried out by gamma spectrometry. This consists on obtaining the spectrum of gamma radiation emitted by different sources and studying the evolution of the peaks (in energetic terms) when concrete plates are



Fig. 1. Appearance and characteristics of the fibers used.

Table 2
Concrete mix proportions (kg/m³).

Component	L-LF-0	L-LF-7P	L-BF-7P	M-0-7P	M-0-40S
CEM	290	278	296	291	291
Water	173	201	207	171	171
NA 12/20	475	455	470	-	-
NA 6/12	475	455	473	-	-
NA 0/6	948	910	859	-	-
MA 0/20	-	-	-	971	971
MA 0/8	-	-	-	2590	2590
BF	-	-	99	-	-
LF	115	114	-	-	-
SF	-	-	-	-	39
PF	-	7	7	7	-
SP	4	4	4	4	4
Fibers (% vol.)	-	0.5	0.5	0.5	0.5
Density (g/cm ³)	2.31	2.27	2.30	3.85	3.88
Slump (mm)	130	120	150	80	150

placed between the source and the detector.

Square plates with 10 cm sides and different thicknesses (0.5–17 cm) have been used, obtaining the linear attenuation coefficient μ (cm⁻¹) as a function of the initial flow intensity (I_0), the final intensity (I) and the thickness of the concrete plate tested (l) according to Lambert's Law (Kazjonovs et al., 2010):

$$I = I_0 e^{-\mu l} \tag{1}$$

In order to characterize the attenuation of concrete for a wide range of photon energy, 4 gamma radiation sources have been used, whose activity and main emission peaks are shown in Table 4. For the ²⁰⁷Bi and ¹³⁷Cs sources, it has not been possible to measure the energies of 75 keV and 32 keV respectively, as the photons of this energy are not detected with the minimum thickness used (0.5 cm). On the other hand, a NaI (TI)

Table 3
Chemical composition of the developed mixes.

Element	L-LF-0	L-LF-7P	L-BF-7P	M-0-7P	M-0-40S
O	47.50%	47.47%	45.36%	34.11%	33.77%
Ca	40.03%	39.91	38.18%	4.58%	4.54%
Si	1.07%	1.06%	1.13%	11.44%	11.34%
Al	0.21%	0.21%	0.22%	4.15%	4.11%
Fe	0.22%	0.22%	0.23%	39.43%	40.09%
S	0.16%	0.16%	0.17%	0.10%	0.10%
K	0.05%	0.05%	0.05%	0.84%	0.83%
Mg	0.09%	0.08%	0.09%	1.44%	1.43%
Ti	0.01%	0.01%	0.01%	0.38%	0.38%
C	10.33%	10.47%	10.77%	0.19%	0.10%
H	0.32%	0.35%	0.37%	0.21%	0.19%
Na	0.01%	0.01%	0.01%	3.15%	3.12%
B	0.00%	0.00%	3.40%	0.00%	0.00%
TOTAL	100.00%	100.00%	100.00%	100.00%	100.00

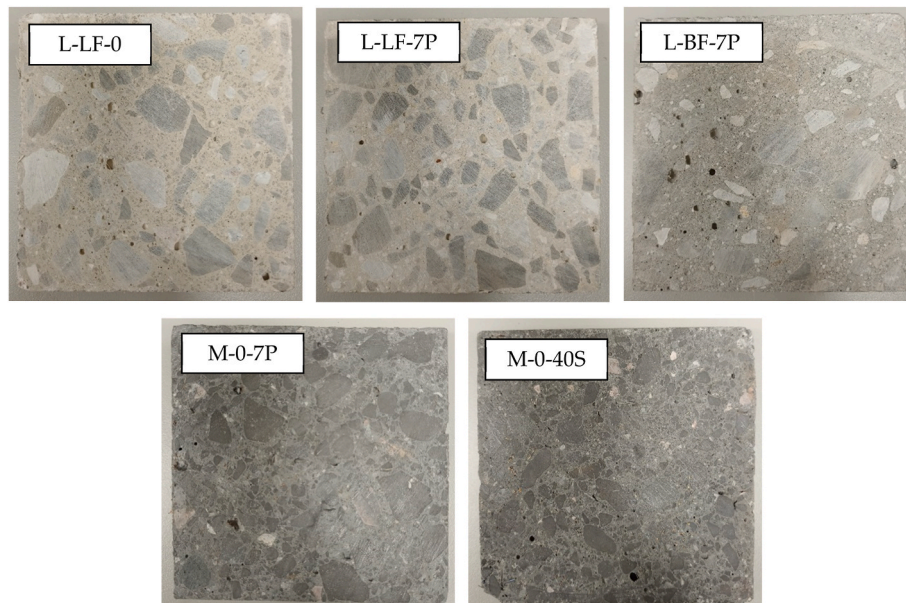


Fig. 2. Aspect of the designed mixes after cutting (100 × 100 mm plates).

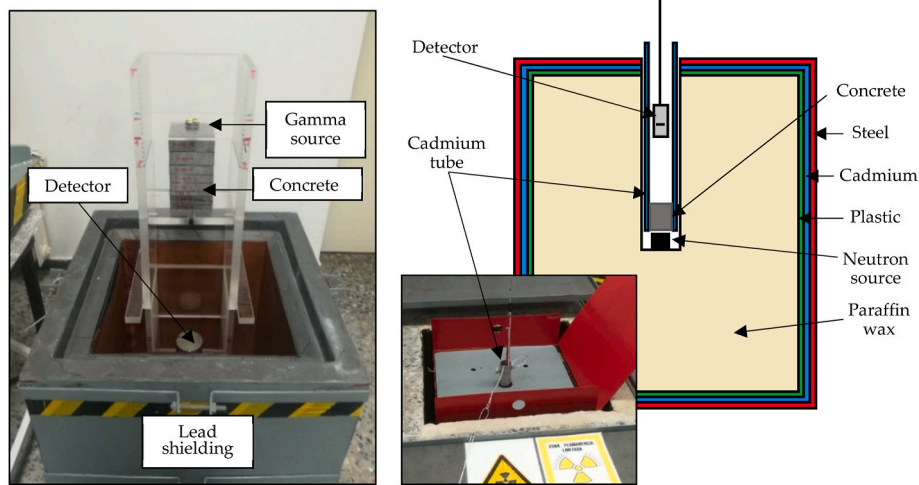


Fig. 3. Experimental set-up for gamma (left) and neutron (right) radiation shielding tests.

Table 4
Characteristics of gamma radiation sources used in research.

Gamma radiation source	Source activity (Bq)	Emission energies (keV)
^{207}Bi	$4.872 \cdot 10^4$	570 1064
^{137}Cs	$7.272 \cdot 10^5$	662
^{60}Co	$3.373 \cdot 10^4$	1170 1330
^{22}Na	$2.623 \cdot 10^5$	511 1280

scintillator detector has been used, whose intrinsic efficiency ranges between 100% and 76% for the range of energies analyzed. The detector is connected to a multichannel analyzer (MCA) and a PC with the necessary software.

In the case of neutron attenuation (Fig. 3 right), cylindrical plates of 4 cm diameter and various thicknesses (0.5–15 cm) have been used. In this case, the attenuation does not occur in a purely exponential way with thickness (not even when considering a monoenergetic beam of neutrons) due to the influence of neutrons scattered mainly in the shielding and, to a lesser extent, in the air until they hit on the detector. This effect is corrected by a factor called “build-up” (Δ), which allows the neutron cross-section Σ (cm^{-1}) to be related to the initial neutron flux (Φ_0), the final neutron flux (Φ) and to the thickness (x) as shown (Price et al., 1957):

$$\Phi(x) = \Phi_0(1 + \Delta(\Sigma x)^2)e^{-\Sigma x} \quad (2)$$

In this case, an Am–Be source has been used, which, as shown in Fig. 3 (right), is located at the bottom of a cadmium tube (used as collimator) that is in turn coated with paraffin wax. The source has an activity of 3 Ci (111 GBq) and the ^{241}Am in contact with the ^9Be generates a flux (Φ) of $6.6 \cdot 10^6$ n/s (in 4π geometry), and whose energy spectrum extends up to 10 MeV. The detector used consists of a silicon photodiode on which a glass support has been placed on which a sheet of lithium fluoride LiF enriched in ^6Li has been deposited, to favor the nuclear reaction $^6\text{Li}(n,\alpha)^3\text{H}$. The efficiency of the detector has been analyzed in another work by the authors (Voytchev et al., 2003).

2.3. Simulations

The simulations of the experimental devices performed with MAVRIC code uses Scale data library to create modelling of complex geometry configurations and calculated particle flux reaching the detector. The Scale nuclear data used (material composition libraries, cross-

sections libraries, etc.) can be consulted in the Scale Manual (ORNL/TM-2005/39 Version 6.2.3, March 2018). MAVRIC can perform deep penetration radiation simulations with automatic variance reduction using adjoint-biased source and importance mapping to improve the Monte Carlo computational speed. Both the radiation sources and the composition and density obtained for the different concrete mixes have been included as input. In this way, it has been possible to reproduce the measurements made in the laboratory and therefore validate the attenuation obtained by the concrete.

Through the gamma set-up model (Fig. 4 left), the measurements made in the laboratory for each concrete have been reproduced using a fictitious gamma source that emits photons in a continuous range of energies from 25 to 17,000 keV (Fig. 4 left). The linear attenuation coefficient μ of the concretes in a wider range of gamma energies has been obtained for each of the 5 concrete mixes. This coefficient has been obtained using Eq. (1), by performing a linear fit with the different thicknesses and fluxes obtained for each energy.

The experimental device for neutron attenuation (Fig. 4 right), has been modeled considering the volumetric neutron source with the Am-241/Be source spectra and a strength of 6.6×10^6 n/s. The detector has been modeled as a hollow steel cylinder inside which is the LiF detector sheet.

Taking the neutron flux calculated in the detector Φ placing concrete plates between the detector and the source, the flux calculated without placing concrete as the incident flow in the concrete Φ_0 , and considering the ^6Li cross section to account the detector efficiency by neutron energy, the adjustment to Eq. (2) has been made. Thus, the values of build-up Δ and Σ (obtained through a fit) are determined using different concrete thicknesses for each concrete mix.

2.4. Model of a spent fuel cask

The validation of the simulations with the experimental results leads to the simulation of more complex geometries that allow comparing the behavior of each mix in terms of total dose rate (sum of the neutron and photon contributions to the dose rate).

Thus, the geometry of a simplified spent nuclear fuel casks has been modeled considering each of the concrete mixes as the cask shielding. The thickness of the concrete shield of each cask has been established so that to ensure that all the modeled casks have same total weight. In all cases, the cask lid has a thickness of 25.5 cm and the base 22 cm. Inside the concrete shield there is a 15 cm thick aluminum case within which 52 positions for the fuel assemblies are located. A homogeneous geometry in the rectangular area of the fuel basket has been considered for the fuel assemblies (Fig. 5).

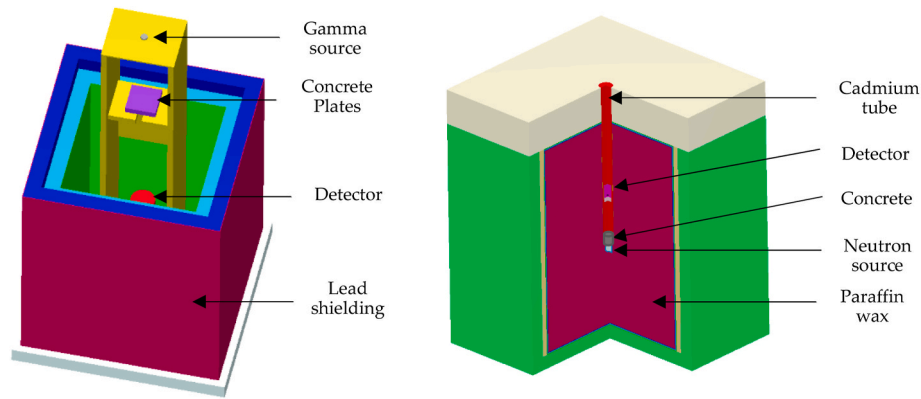


Fig. 4. MAVRIC models of the devices for gamma (left) and neutron (right) attenuation tests.

In the same way, for the spent fuel cask, in the calculations of the spent nuclear fuel source term with ORIGEN-ARP (SCALE 6.1. package), the libraries of standard effective cross-sections available in Scale, calculated for certain range of burn-up and enrichment, are used. From these libraries, the ARP sequence interpolates the specific libraries for the data entered as input, and uses the templates available for the design of the fuel assembly selected (in this case, the ge8x8-4 template for the GE6 design). The following hypotheses have been taken into account:

- 27 energy groups for the neutron source term and 19 energy groups for the gamma source term.
- A single burn cycle to discharge burn (no shutdown between cycles).
- A void fraction of 40%.
- The density of the fuel rods and the axial enrichment are assumed constant.
- Activation of structural components are not considered.

The type of fuel assembly selected (GE6), has an initial enrichment of 2.8%, assuming that each element has been operating with a constant power of 4.33 MW and with a burnup of 37,500 MWd/MtU. The cooling time has been assumed to be 22.5 years. The mass of uranium used was 0.18145 tons per fuel assembly. An axial emission profile has been considered to account the different burns along the axial height of the FAs and form factors of 1.045 and 1.602 have been used for the gamma and neutron source terms, respectively.

Using these models, the dose rate (mSv/h) due to both neutrons and photons in contact with the cask and at 1, 2, 5, 10 and 50 m from the

cask external surface has been calculated. To carry out these calculations, several cylindrical meshes with sufficient radial, azimuthal and axial intervals have been defined around the cask, and the dose rate has been calculated in each of the zones delimited by the ends of said intervals (meshtally). Thus, all the dose rate values can be analyzed and the maximum value for the different distances is obtained.

3. Results and discussions

3.1. Gamma radiation attenuation

The effectiveness of a material in attenuating photons depends on its density, as shown in Fig. 6 for a photon energy of 1332 keV. It can be seen how other authors (Pomaro et al. (2019), Piyapong et al. (Suwanmaneechot et al., 2021)) obtain a very similar fit to the one obtained in the experimental tests for concrete, validating the data obtained. A slight underestimation is also observed in the calculations made by the simulation and that allows obtaining results that are on the side of safety. This underestimation can be estimated at around 0.01 cm^{-1} on average for the entire spectrum of densities analyzed.

The agreement between experimental results and simulations is shown in Fig. 7 (left) as well as in Fig. 7 (right), where the energy range of 500–1400 keV is shown. An acceptably high correspondence is observed that allows validating the assumptions made to run the simulations. This check allows to validate geometrically more complex models, such as a cask for spent nuclear fuel storage.

Fig. 7 shows the differences between the concretes that incorporate

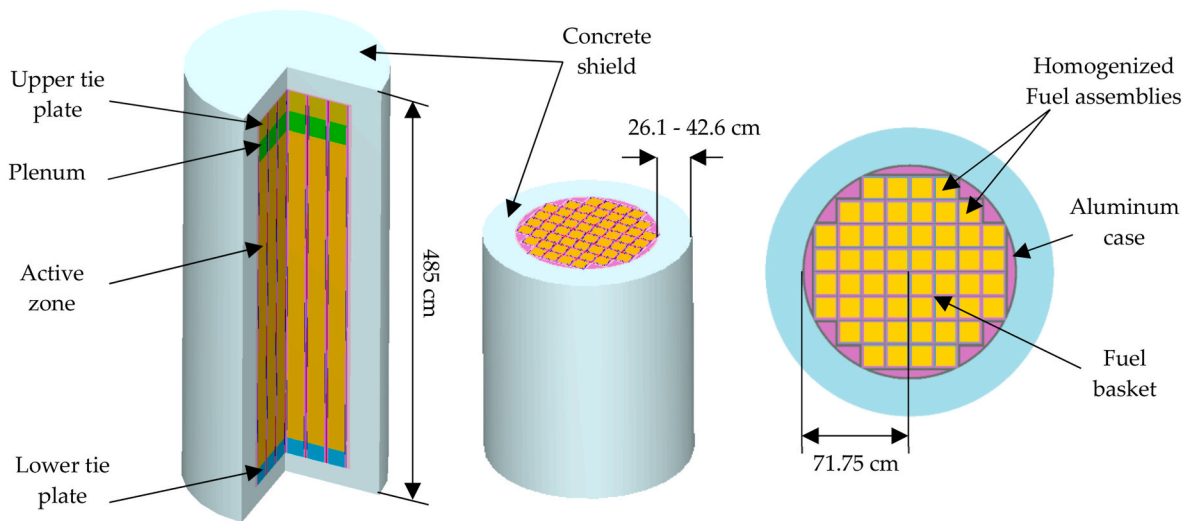


Fig. 5. Simplified model of a spent fuel cask.

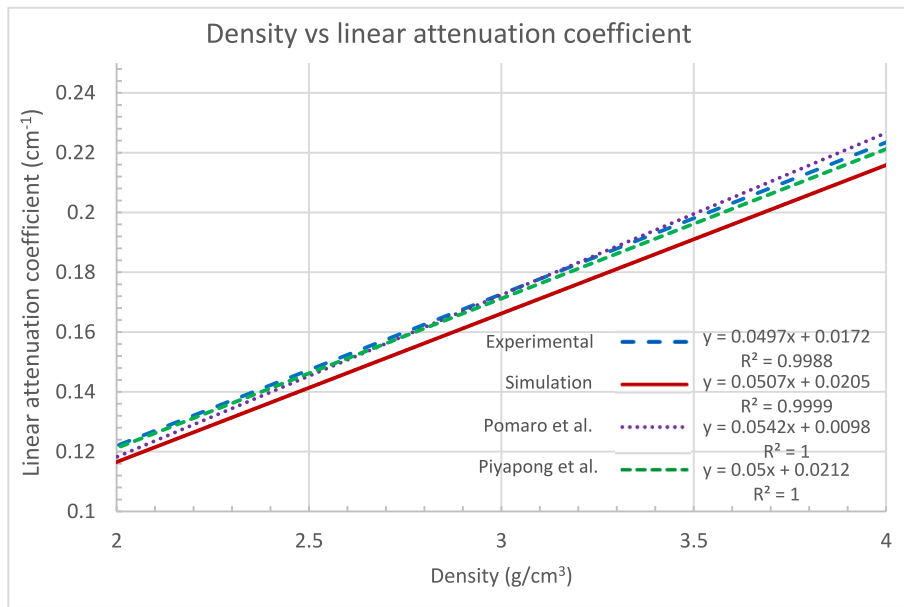


Fig. 6. Relationship between density and linear attenuation coefficient (1332 keV).

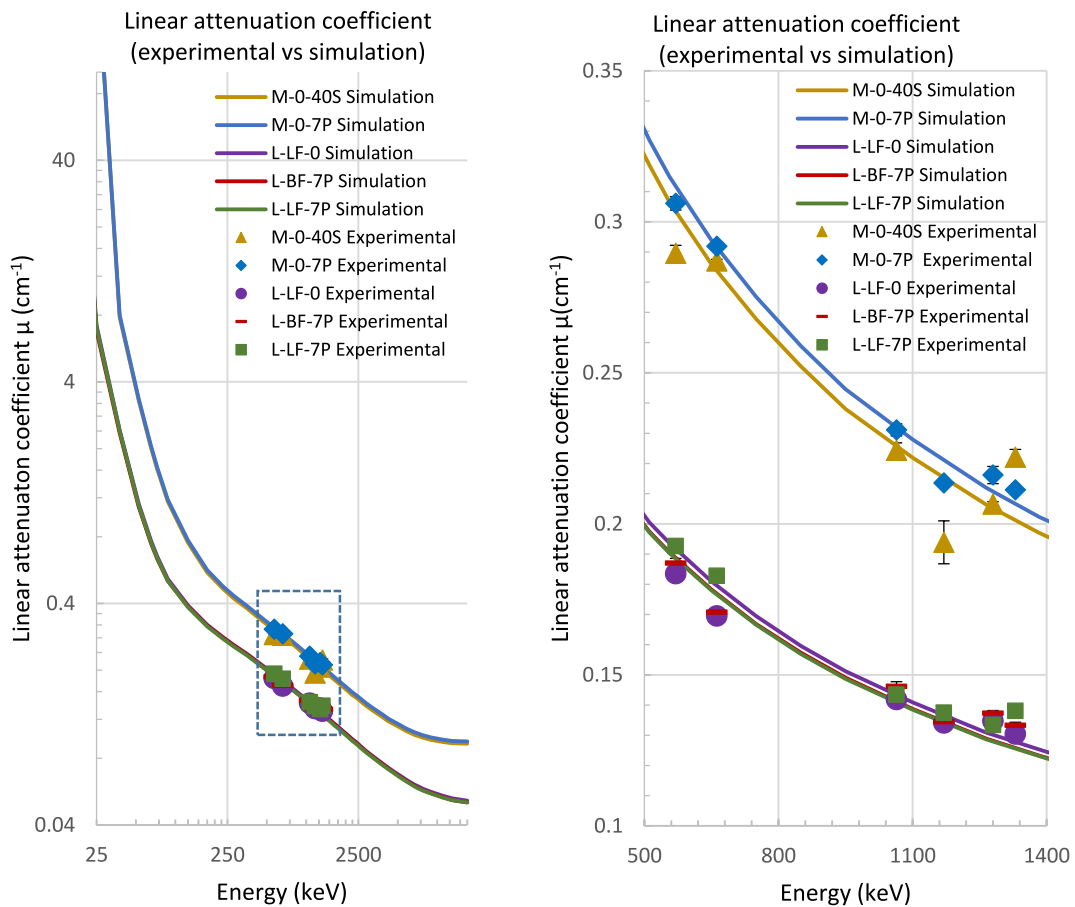


Fig. 7. Linear attenuation coefficient (μ) as a function of energy (left) and magnification of the selected area (right).

different aggregates and fibers. Note that μ is proportional to the energy of the photons in the energy range where the Compton effect predominates ($\sim 1\text{--}10$ MeV) for elements of low and intermediate atomic numbers. On the other hand, in Fig. 7 (left) it can be clearly distinguished between the concretes that incorporate limestone aggregates

and magnetite, which describe two easily distinguishable lines with two behavior patterns. Fig. 7 (right) shows that the concrete mixes L-LF-7P and L-BF-7P have a very similar attenuation capacity (in fact only a green line is visible, which overlaps with the red line), while the reference concrete L-LF-0 shows a significantly higher shielding capacity, due

to the fact that the density of the limestone aggregate is higher than that of the PVA fibers and that of the boron carbide filler.

The mixes that incorporate magnetite have a linear attenuation coefficient that is on average a 60% higher than concrete with limestone aggregates for the energy range of 250–2500 keV. This difference increases for energies of 10,000 keV, a region where the production of pairs begins to be predominant. The differences found in the effectiveness of gamma radiation attenuation can be expressed in terms of the thickness of the half-value layer (HVL), which reaches 4.5 cm for

concrete with limestone and 2.8 cm for concrete with magnetite for energies of 1000 keV (60% lower). Regarding uncertainties, values between 1% and 3% have been reported in all cases, although in the plots of Fig. 8, what is presented is the linear attenuation coefficient resulting from fitting the above data to a curve. The error represented in this case is that obtained in the fit, and is for all cases less than 1.5% (almost not visible).

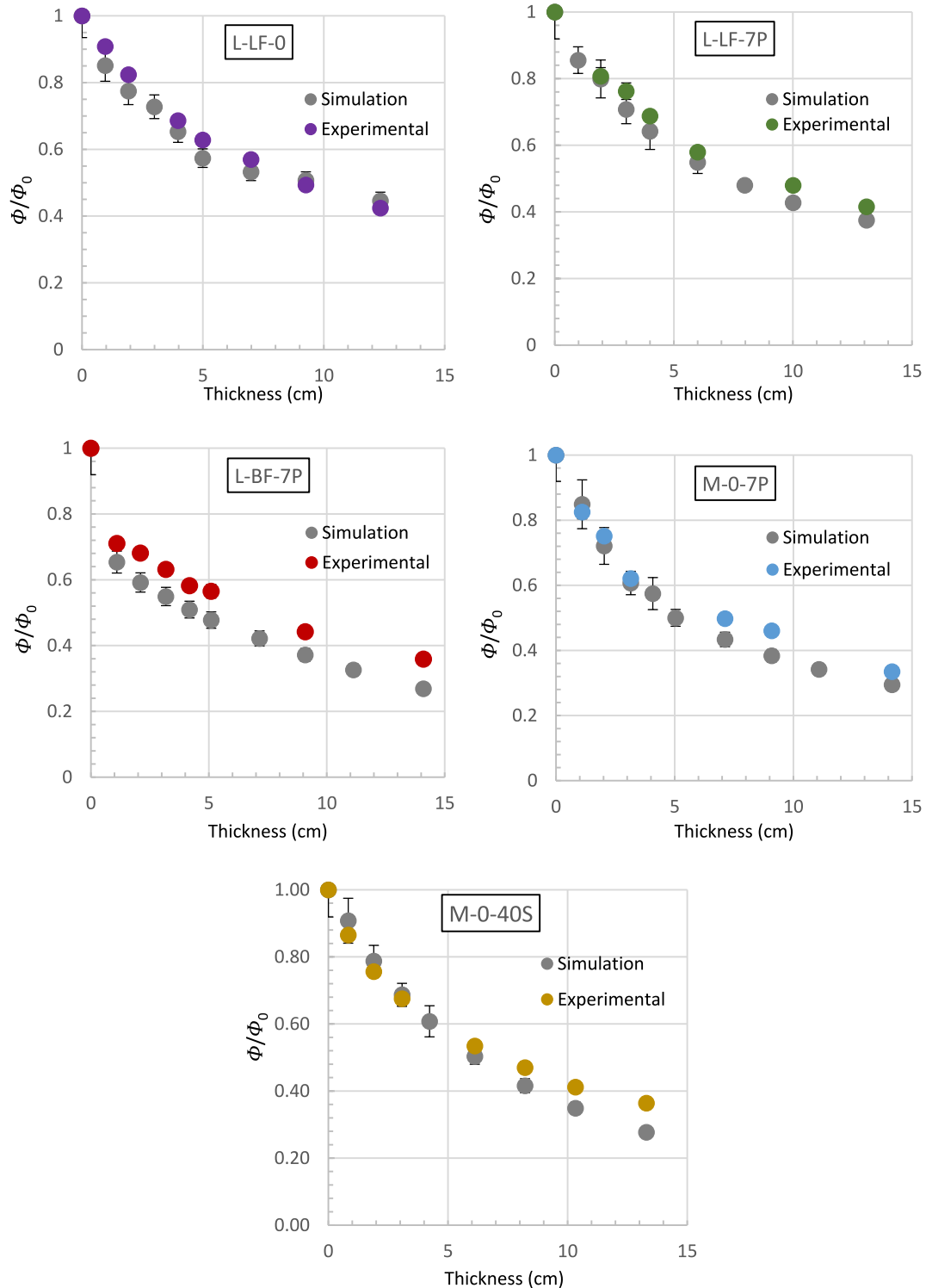


Fig. 8. Neutron attenuation as a function of thickness.

3.2. Neutron attenuation

The effectiveness of a shield against fast neutrons will depend on the content of atoms with light nuclei (moderators/thermalizers) and absorbing elements, in addition to the density of the material. Fig. 8 shows, individually, the results obtained through the simulations (using the experimental device) and experimental tests. A priori, the simulations are quite consistent with the experimental results, although they overestimate the attenuation of the mixes that incorporate magnetite for thicknesses greater than 5 cm and the attenuation of the mix that incorporates boron carbide (L-BF-7P). For this last mix, it is observed that for the first thickness (1 cm) an attenuation factor of around 0.70 has been obtained, when in the rest of the mixes it oscillates around 0.84–0.88. This demonstrates the effectiveness of boron for small thicknesses.

On the other hand, Table 5 shows the Σ and Δ obtained for the 5 mixes developed using the simulation of the experimental device and the data from the experimental device itself. It is surprising that Σ even doubles when incorporating 100 kg/m^3 of BF, demonstrating the enormous efficiency of this filler for these applications.

A good correlation is obtained between experimental and theoretical results as, in both cases, the same trend is observed for the mixes, although the simulation tends to overestimate the attenuation capacity of the material by about 25%. No positive effect on the use of polymeric fibers is observed and, in the comparison between magnetite aggregate and limestone (without taking BF into account), the results are slightly favorable to the former.

Finally, it is important to note that there are tradeoffs between the effects on gamma and neutron shielding. While the inclusion of materials such as boron carbide may greatly enhance neutron shielding, it may simultaneously reduce gamma shielding efficiency. Similarly, the impact of PVA fibers on neutron cross sections may be minimal, but they could positively influence other properties such as flexural strength and fire resistance, which are crucial in accident scenarios. Additionally, the mechanical effects of steel fibers on concrete are comparable to polymer fibers, albeit with the added benefit of increased density. These nuances highlight the multifaceted nature of material selection for concrete shielding applications, where various factors must be considered beyond just density.

3.3. Attenuation of a spent fuel cask

Fig. 9 shows simulation results of the photon dose rates as a function of the distance from the cask for all the mixes developed. The dose rates in contact with the cask surface are highly variable depending on the mixes, being reduced by a 10–14% when high-density mixes are used (M-0-40S and M-0-7P, whose lines practically overlap). This reduction increases with the distance to the cask up to 15–22% since, at long distances, the contribution due to the air scattering of the cask top lid leakage becomes more important and that, for all mixes, the top lid has been considered with the same thickness regardless their density.

For neutron fluxes, the neutron dose rates have been obtained as a function of the distance shown in Fig. 10. There are greater differences between mixes than those obtained for photon dose rates, since dose rates in contact are reduced up to almost 80% between the M-0-40S (less

effective) and the L-BF-7P (greater effective). The effect of boron carbide is very notable also compared with the limestone aggregate, obtaining a reduction of dose rates in contact with the cask of more than a 50%. The PVA fibers are responsible for a 7–13% decrease in neutron dose rate when they are incorporated into the concrete. In contrast to photons, the reduction in dose rates decreases slightly with distance, although borated concrete remains in all cases the most effective neutron barrier.

Finally, the total dose rate (neutron dose rate + photon dose rate) is shown in Fig. 11. Additionally, the contribution of each source to the total dose rates obtained is presented in Fig. 12 for each mix. It is observed that the dose rate generated by photons is between 1 and 2 orders of magnitude greater than that of neutrons, so that for the source term used, it seems more effective to use a high-density concrete than a borated concrete. However, with the use of limestone aggregates, the neutron contribution to the total dose rate is reduced by half in comparison with high-density concretes. This contribution is further reduced with bored concrete to values below 1%.

Solutions to reduce these dose rates would include increasing the thickness of the concrete shielding, which is currently between 26 and 42 cm depending on the density of the mix, to obtain a shielding of equal weight (29.1 t). The use of shielding of the same thickness would increase the shielding capacity of mixes with magnetite with respect to mixes with limestone aggregate.

4. Conclusions

In this research, the effect of incorporating fibers, both polymeric and metallic, into the cement matrix, in terms of radiological shielding capacity, has been revealed. The effect of incorporating boron carbide in the concrete has also been revealed, as well as evaluating the effect of using conventional and dense aggregates for its manufacture. The means to characterize this behavior include an experimental device, modeling of the experimental device with MAVRIC® and, once these have been validated, the modeling of a simplified spent nuclear fuel cask. After analyzing the results, the following conclusions can be drawn:

- Experimental device tests and simulations:
 - The results with the experimental device have allowed validating the results of the simulations both in terms of μ and Σ .
 - Σ even doubles when incorporating 100 kg/m^3 of BF, demonstrating the enormous efficiency of this filler for these applications.
 - Incorporating PVA fibers instead of steel fibers, with the consequent decrease in density, does not provide an improvement in the attenuation capacity of concrete with magnetite. The same applies when PVA fibers are incorporated into limestone concrete.
- Cask shielding calculations (keeping the same cask mass for all mixes):
 - The incorporation of any type of fibers has a negligible effect on the photon dose rate generated by the cask model beyond that produced by the change in density.
 - A slight positive effect in neutron attenuation is observed with the use of PVA fibers and the effect of boron carbide on the neutron dose rate results in a reduction of more than 50% of the dose rate in contact with the cask compared to other limestone mixes.

Table 5

Values of Σ and Δ obtained in the simulations and with the experimental device.

Mix	Simulation				Experimental			
	Σ	Error	Δ	Error	Σ	Error	Δ	Error
L-LF-7P	0.125	1.94E-03	0.381	1.65E-03	0.096	6.58E-03	0.268	3.20E-02
L-LF-0	0.140	9.84E-03	0.466	2.81E-02	0.101	2.12E-04	0.262	1.53E-02
M-0-7P	0.158	3.66E-03	0.374	2.35E-02	0.148	9.94E-03	0.483	3.46E-02
M-0-40S	0.180	2.29E-02	0.111	2.53E-02	0.151	7.01E-03	0.403	1.02E-02
L-BF-7P	0.279	3.96E-02	0.695	5.16E-02	0.210	3.72E-02	0.728	5.27E-02

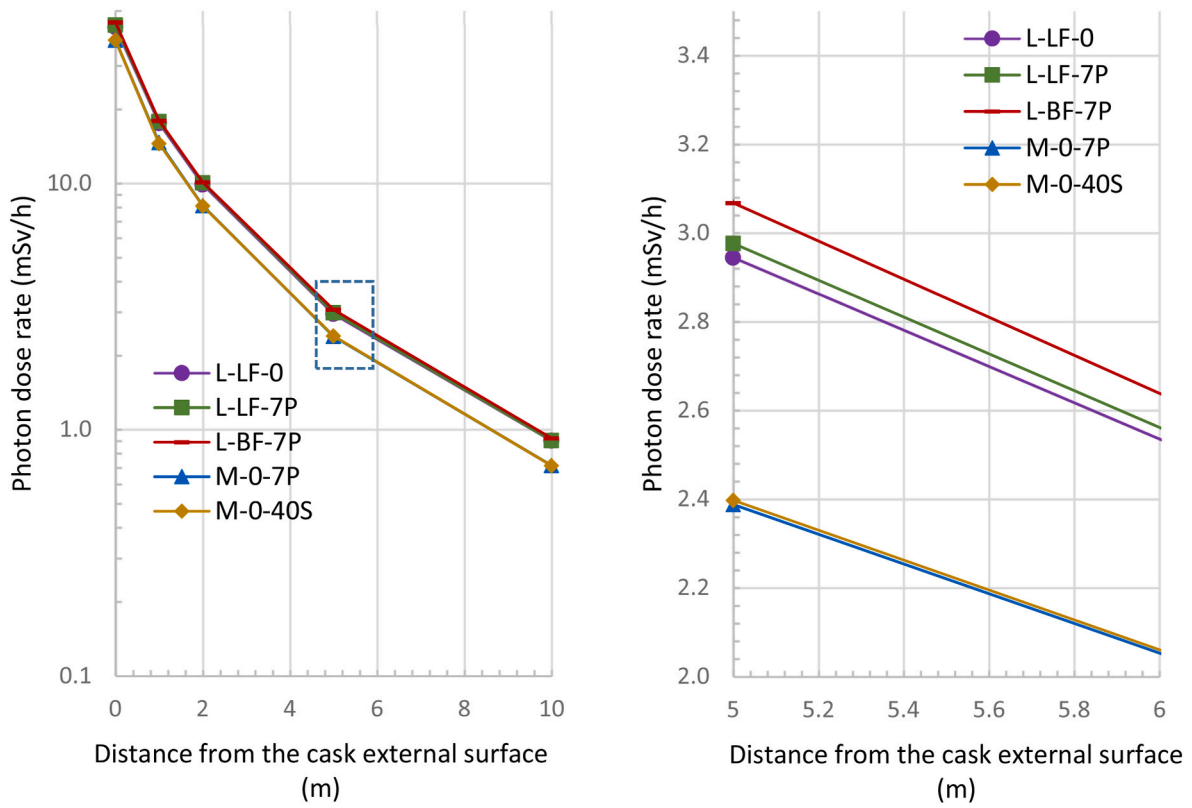


Fig. 9. Photon dose rate as a function of distance to the cask (left) and magnification of the selected area (right).

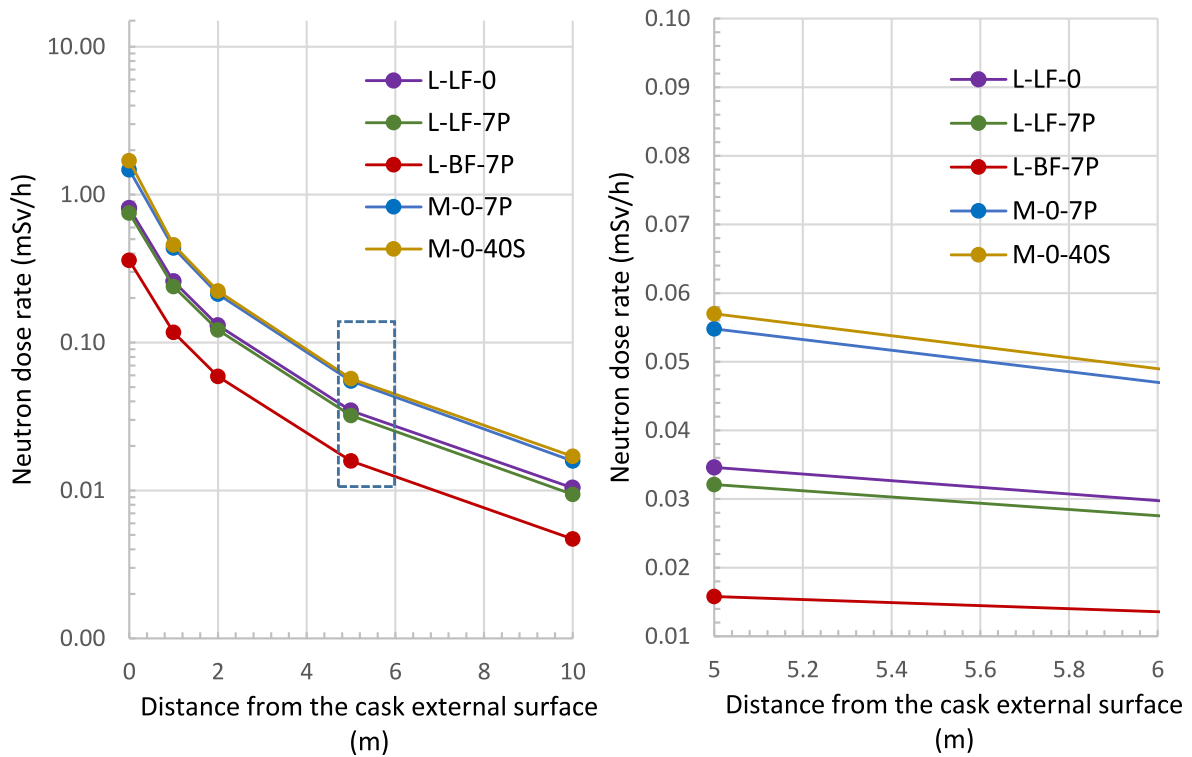


Fig. 10. Neutron dose rate as a function of distance from the cask (left) and magnification of the selected area (right).

o The total dose rate generated by photons is between 1 and 2 orders of magnitude greater than that of neutrons, so that for the source term used, it seems more effective to use a high-density concrete than a borated concrete.

CRedit authorship contribution statement

S. Pérez: Methodology, Investigation, Formal analysis, Data curation, Conceptualization. P. Tamayo: Writing – review & editing, Writing

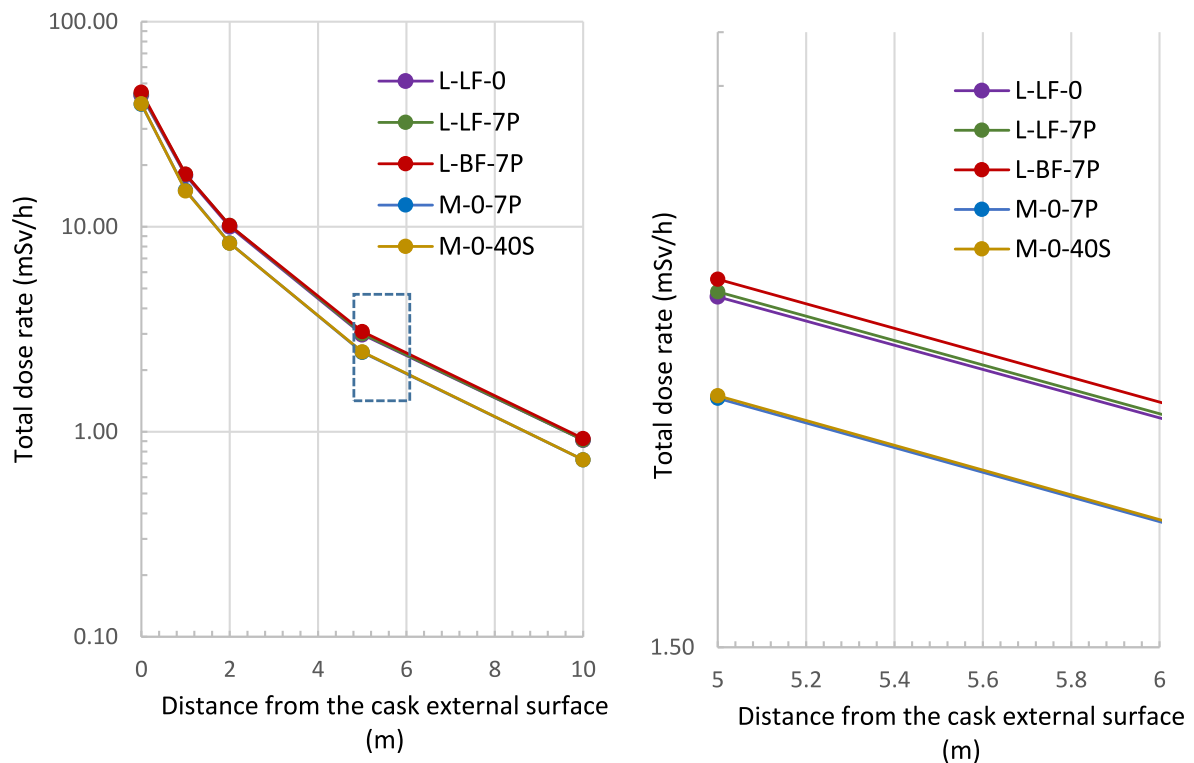


Fig. 11. Total dose rate as a function of distance from the cask (left) and magnification of the selected area (right).

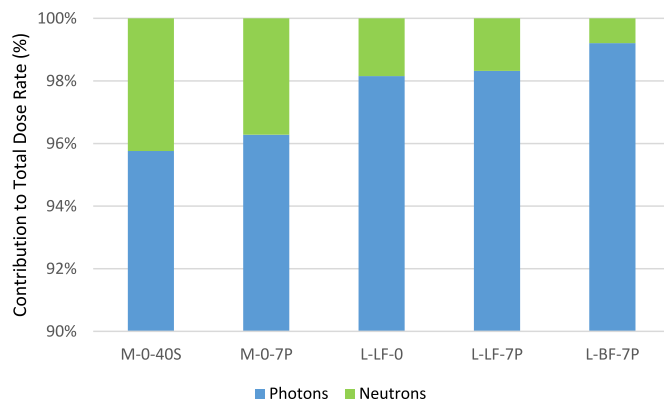


Fig. 12. Contribution to the total dose rate of the neutron and photon sources for the different mixes in contact with the cask.

– original draft, Supervision, Investigation, Formal analysis, Data curation, Conceptualization. **J. Rico:** Supervision, Resources, Project administration, Methodology, Funding acquisition, Conceptualization. **J. Alonso:** Supervision, Software, Project administration, Methodology, Conceptualization. **C. Thomas:** Writing – review & editing, Validation, Supervision, Project administration, Methodology, Formal analysis.

Declaration of competing interest

The authors declare the following financial interests/personal relationships which may be considered as potential competing interests: Sara Perez reports was provided by Construction Engineering, Research and Project Development (INGECID S.L.).

Data availability

No data was used for the research described in the article.

Acknowledgments

This research was co-financed by the European Regional Development Fund (ERDF) and the Ministry of Economy, Industry and Competitiveness (MINECO) within the framework of the project RTC-2016-5637-3. The research has been possible thanks to the collaboration of the company INGENIC, the department LADICIM (University of Cantabria) the Modern Physics Department of the University of Cantabria and the companies ROCACERO and SIDENOR.

References

- AENOR, 2008a. EN 14889-1: Fibres for Concrete - Part 1: Steel Fibres - Definitions, Specifications and Conformity.
- AENOR, 2008b. EN 14889-2: Fibres for Concrete - Part 2: Polymer Fibres - Definitions, Specifications and Conformity.
- Al-Ghamdi, H., Elsafi, M., Sayyed, M.I., Almuqrin, A.H., Tamayo, P., 2022. Performance of newly developed concretes incorporating WO₃ and barite as radiation shielding material. *J. Mater. Res. Technol.* 19, 4103–4114.
- Ameri, F., de Brito, J., Madhkan, M., Taheri, R.A., 2020. Steel fibre-reinforced high-strength concrete incorporating copper slag: mechanical, gamma-ray shielding, impact resistance, and microstructural characteristics. *J. Build. Eng.* 29, 101118 <https://doi.org/10.1016/j.jobe.2019.101118>.
- British Standards Institution, 1998. Tests for Mechanical and Physical Properties of Aggregates - Part 3: Determination of Loose Bulk Density and Voids.
- Çakıroğlu, M.A., 2016. Investigation of radiation shielding properties of polypropylene fiber reinforced shotcrete. *Acta Phys. Pol., A* 129, 705–706.
- El-Sayed Abdo, A., 2002. Calculation of the cross-sections for fast neutrons and gamma-rays in concrete shields. *Ann. Nucl. Energy* 29, 1977–1988. [https://doi.org/10.1016/S0306-4549\(02\)00019-1](https://doi.org/10.1016/S0306-4549(02)00019-1).
- E.N. 1097-6:2014, 2014. Tests for Mechanical and Physical Properties of Aggregates - Part 6: Determination of Particle Density and Water Absorption.
- E.N. 12350-2:2009, 2009. Testing Fresh Concrete - Part 2: Slump-Test.
- E.N. 12390-7:2009, 2009. Testing Hardened Concrete - Part 7: Density of Hardened Concrete.
- E.N. 197-1:2011, 2011. Cement - Part 1: Composition, Specifications and Conformity Criteria for Common Cements.
- Kaplan, M.F., 1989. Concrete Radiation Shielding.
- Kazjonovs, J., Bajare, D., Korjakins, A., 2010. Designing of high density concrete by using steel treatment waste. In: 10th Int. Conf. Mod. Build. Mater. Struct. Tech., pp. 138–142.

- Khaloo, A., Molaei Raisi, E., Hosseini, P., Tahsiri, H., 2014. Mechanical performance of self-compacting concrete reinforced with steel fibers. *Construct. Build. Mater.* 51, 179–186. <https://doi.org/10.1016/j.conbuildmat.2013.10.054>.
- Mehta, P.K., Monteiro, P.J.M., 2006. *Concrete: Microstructure, Properties, and Materials*. Peng, Y.-C., Hwang, C.-L., 2011. Development of high performance and high strength heavy concrete for radiation shielding structures. *Int. J. Miner. Metall. Mater.* 18, 89–93.
- Pomaro, B., Gramegna, F., Cherubini, R., De Nadal, V., Salomoni, V., Faleschini, F., 2019. Gamma-ray shielding properties of heavyweight concrete with Electric Arc Furnace slag as aggregate: an experimental and numerical study. *Construct. Build. Mater.* 200, 188–197.
- Price, B.T., Horton, C.C., Spinney, K.T., 1957. *RADIATION SHIELDING in the International Series of Monographs on Nuclear Energy*.
- Roslan, M.K.A., Ismail, M., Kueh, A.B.H., Zin, M.R.M., 2019. High-density concrete: exploring Ferro boron effects in neutron and gamma radiation shielding. *Construct. Build. Mater.* 215, 718–725.
- Sarkawi, M.S., Zain, M.R.M., Rabir, M.H., Idris, F.M., Zainal, J., 2018. Radiation shielding properties of ferro-boron concrete. In: *IOP Conf. Ser. Mater. Sci. Eng.* IOP Publishing, 12037.
- Singh, K., Singh, S., Dhaliwal, A.S., Singh, G., 2015. Gamma radiation shielding analysis of lead-flyash concretes. *Appl. Radiat. Isot.* 95, 174–179.
- Suwanmaneehot, P., Bongkarn, T., Joyklad, P., Julphunthong, P., 2021. Experimental and numerical evaluation of gamma-ray attenuation characteristics of concrete containing high-density materials. *Construct. Build. Mater.* 294, 123614.
- Tamayo, P., Thomas, C., Rico, J., Cimentada, A., Setién, J., Polanco, J.A., 2020. Review on neutron-absorbing fillers. In: *Micro Nanostructured Compos. Mater. Neutron Shield. Appl.* Elsevier, pp. 25–52.
- Tamayo, P., Thomas, C., Rico, J., Pérez, S., Mañanes, A., 2022. Radiation shielding properties of siderurgical aggregate concrete. *Construct. Build. Mater.* 319, 126098 <https://doi.org/10.1016/j.conbuildmat.2021.126098>.
- Thomas, C., Rico, J., Tamayo, P., Ballester, F., Setién, J., Polanco, J.A., 2019a. Effect of elevated temperature on the mechanical properties and microstructure of heavy-weight magnetite concrete with steel fibers. *Cem. Concr. Compos.* 103, 80–88.
- Thomas, C., Rico, J., Tamayo, P., Setién, J., Ballester, F., Polanco, J.A., Setién, J., Polanco, J.A., 2019b. Neutron shielding concrete incorporating B4C and PVA fibers exposed to high temperatures. *J. Build. Eng.* 26, 100859.
- Thomas, C., Tamayo, P., Setien, J., Ferreno, D., Polanco, J.A., Rico, J., 2021. Effect of high temperature and accelerated aging in high density micro-concrete. *Construct. Build. Mater.* 272, 121920.
- Tyagi, G., Singhal, A., Routroy, S., Bhunia, D., Lahoti, M., 2020. A review on sustainable utilization of industrial wastes in radiation shielding concrete. *Mater. Today Proc.* 32, 746–751.
- Voytchev, M., Iniguez, M.P., Méndez, R., Mañanes, A., Rodríguez, L.R., Barquero, R., 2003. Neutron detection with a silicon PIN photodiode and 6LiF converter. *Nucl. Instruments Methods Phys. Res. Sect. A Accel. Spectrometers, Detect. Assoc. Equip.* 512, 546–552.
- Yarar, Y., Bayülken, A., 1994. Investigation of neutron shielding efficiency and radioactivity of concrete shields containing colemanite. *J. Nucl. Mater.* 212, 1720–1723.